mathematics

MDPI

Article

A Time–Space Numerical Procedure for Solving the Sideways Heat Conduction Problem

Ching-Chuan Tan, Chao-Feng Shih, Jian-Hung Shen and Yung-Wei Chen *

Department of Marine Engineering, National Taiwan Ocean University, Keelung 202301, Taiwan; 20566001@mail.ntou.edu.tw (C.-C.T.); joushning@gmail.com (C.-F.S.); 20666006@email.ntou.edu.tw (J.-H.S.)
* Correspondence: cyw0710@mail.ntou.edu.tw; Tel.: +886-2-24622192 (ext. 7133)

Abstract: This paper proposes a solution to the sideways heat conduction problem (SHCP) based on the time and space integration direction. Conventional inverse problems depend highly on the available data, particularly when the observed data are contaminated with measurement noise. These perturbations may lead to significant oscillations in the solution. The uniqueness of the solution in this SHCP requires revaluation when boundary conditions (BCs) or initial conditions (ICs) are missing. First, the spatial gradient between two points resolves the missing BCs in the computational domain by a one-step Lie group scheme. Further, the SHCP can be transformed into a backward-in-time heat conduction problem (BHCP). The second-order backward explicit integration can be applied to determine the ICs using the two-point solution at each time step. The performance of the suggested strategy is demonstrated with three numerical examples. The exact solution and the numerical results correspond well, despite the absence of some boundary and initial conditions. The only method of preventing numerical instability in this study is to alter the direction of numerical integration instead of relying on regularization techniques. Therefore, a numerical formula with two integration directions proves to be more accurate and stable compared to existing methods for the SHCP.

Keywords: sideways heat conduction problem (SHCP); backward heat conduction problem (BHCP); Lie group shooting method (LGSM)

MSC: 35K20

check for updates

Academic Editors: Erwin Suazo and Jose M. Vega-Guzman

Received: 21 January 2025
Revised: 22 February 2025
Accepted: 24 February 2025
Published: 25 February 2025

Citation: Tan, C.-C.; Shih, C.-F.; Shen, J.-H.; Chen, Y.-W. A Time–Space Numerical Procedure for Solving the Sideways Heat Conduction Problem. *Mathematics* **2025**, *13*, 751. https://doi.org/10.3390/math13050751

Copyright: © 2025 by the authors. Licensee MDPI, Basel, Switzerland. This article is an open access article distributed under the terms and conditions of the Creative Commons Attribution (CC BY) license (https://creativecommons.org/licenses/by/4.0/).

1. Introduction

Many engineering systems involve harsh high-temperature environments and have certain characteristics that prevent direct temperature measurement. Therefore, using inverse analysis to determine their effects is very important and necessary. For example, the initial temperature of heat exchangers on ships has a crucial impact on the operation and efficiency of boilers. Preheating the feed water can reduce the precipitation of dissolved gases and minerals, thereby reducing the risk of boiler scaling. A higher initial temperature can remove these impurities before entering the boiler, thereby improving steam quality and boiler efficiency. It can also ensure the stability and quality of the steam supply, thereby improving the overall performance of the steam system. The inverse heat conduction problem (IHCP) can simply and accurately determine the absorption heat flux, internal heat transfer, combustion water wall coefficient and fluid temperature cavity [1] and improve the efficiency of the heat exchanger chip [2]. Regularly monitoring the heat flux and temperature distribution in boiler pipes can help detect scaling or deposition issues in a timely manner. Properly managing boiler heat flux and scaling problems can not only improve the

boiler's thermal efficiency but also reduce maintenance costs and extend the equipment's lifespan. Subsurface temperature measurements are additionally employed to calculate the surface heat flux distribution, helping to solve the IHCP related to the application of thermal barrier coatings (TBCs) on internal combustion engine cylinders [3]. When the boundary conditions (BCs), initial conditions (ICs), and material parameters are fully specified, the proposed calculation method accurately predicts the internal temperature of the studied system. When dealing with unfamiliar ICs, BCs, material properties, or the inability to monitor temperature or heat flux, it becomes necessary to measure the temperature at specific locations within the material to identify temperature, heat flux, or material qualities at a given position.

According to Hadamard [4], the criteria for existence, uniqueness, and continuous dependence are violated in these inverse problems. Solving the IHCP is more challenging than solving the direct heat conduction problem (DHCP). Predicting temperature distribution, heat flux distribution, and associated heat transfer processes are all integral components of solving the IHCP, and ICs and BCs are typically required to ensure the uniqueness of the solution [5,6]. The challenge of formulating the inverse problem is effectively addressed by simultaneously reconstructing the surface and domain heat transfer coefficients (HTCs) and deriving the initial temperature from measurements at two different time points [7]. To distinguish the SHCP from other types of IHCPs, this paper will focus on the SHCP.

Beck and Blackwell [8] propose an effective regularization method that improves the accuracy and stability of the IHCP solution. Carasso [9] studied the regularization and convergence of iterative methods for nonlinear, ill-posed problems. Murio [10,11] is based on the finite difference method (FDM) to solve the IHCP. The mollification method significantly improves both the accuracy and computational efficiency of numerical solutions for ill-posed problems. Al-Khalidy [12] proposed a convergent space-marching algorithm used to estimate the convergence rate for solving the two-dimensional the IHCP. In the context of the FDM using space-marching techniques, Eldén [13] noted that the regularization effect of time discretization, combined with Fourier transform techniques, helps prevent high-frequency noise amplification, thereby enhancing the accuracy of numerical solutions to inverse problems. Moreover, Krutz et al. [14] determined the heat flux, or surface temperature, of a body from measurements of the temperature inside the body, utilized the finite element method (FEM) to solve both steady-state and transient IHCPs. An inverse method was employed to experimentally determine the distribution of the transient heat transfer coefficient on the circular fins of a staggered finned heat exchanger assembly [15]. It offers accurate data support, improving the efficiency and reliability of heat exchangers, while also contributing to ship energy conservation, emission reduction, and technological innovation, thus reducing operating costs and enhancing competitiveness. Reinhardt [16] extended Beck's method to address two spatial dimensions and utilized future times to stabilize the ill-posed IHCP. Numerical methods cannot fully overcome the inherently unstable nature of inverse problems, demonstrating the limitations of using numerous elements in FEM and FDM.

To avoid element discretization in the study of IHCPs, the boundary element method (BEM) was further developed. For example, Brebbia [17] first applied and demonstrated the effectiveness and superiority of BEM in solving IHCPs. Many researchers, such as Pasquetti et al. [18], Ingham et al. [19], and Kurpisz and Nowak [20], have further developed various BEM formulations to overcome the ill-posed inverse problems. Furthermore, Lesnic [21] combined the BEM with the minimum energy technique to compute the temperature distribution and heat flux on the remaining boundaries of the IHCP. Al-Najem et al. [22] proposed a hybrid technique for solving the steady two-dimensional IHCP that combines the BEM, singular value decomposition, integral transform methods, and a least squares

method. Singh and Tanaka [23] proposed the dual reciprocity boundary element method coupled with iterative regularization for solving a transient IHCP. Subsequently, to improve numerical accuracy without requiring domain or boundary discretization, meshless methods [24,25] were proposed to address the IHCP. In summary, although the BEM does not require discretization of the computational domain and can provide temperature data for internal points, its use reduces computational time and storage compared to the FEM and the FDM. However, numerical instability problems may persist. In addition to discrete techniques, various solution methods, such as the wavelet method [26,27], Fourier analysis [28,29], and the sequential method [30,31], have been proposed to construct solutions for the IHCP. By properly considering time, spatial discretization, and continuity, one can avoid ill-posedness and numerical instability, ensuring the existence, uniqueness, and continuous dependence of the solution. Therefore, whether studying the DHCP or IHCP, numerical stability must be preserved, as it is the primary goal of discretization techniques.

To satisfy the well-posed conditions and ensure numerical stability, Liu [32,33] and Liu et al. [34] first proposed the forward and backward group preserving schemes (GPSs) to address the IHCP, incorporating a numerical method with physical architecture. Chang et al. [35] utilized the explicit GPS to tackle the SHCP. However, numerical oscillations still occurred at the unresolved BCs, necessitating the use of ICs to constrain the solution. To eliminate numerical integration, Chang et al. [36] and Chang et al. [35] applied the Lie group shooting method (LGSM) [37], derived from an augmented GPS system, to solve BHCPs. However, the original LGSM with a minimal regularization parameter [35,36] cannot avoid numerical instability when the time span increases. To address this issue, Chen [38,39] utilized ICs and final conditions (FCs) and modified the LGSM by incorporating a minimum weight factor to resolve both homogeneous and nonhomogeneous multidimensional BHCPs. Although the modified LGSM can partially address the long-term inverse calculation issue, error propagation remains unavoidable when handling nonhomogeneous boundary conditions over time. Chen [40] derived a vector two-point solution of the LGSM to simultaneously obtain the ICs and source terms of BHCPs. Chang et al. [41] investigated the Burgers equation at high Reynolds numbers by employing the vector two-point solution of the LGSM. Therefore, based on a vector two-point boundary solution results obtained using the LGSM, it is evident that the boundary missing problems in both two-dimensional and three-dimensional problems can be effectively addressed using the BEM. In addition, Liu [42–45] proposed an adaptive Lie group method (LGAM) for recovering the spatially dependent and time-dependent thermal conductivity function from the nonlinear heat conduction equation. Hence, whether using a scalar or a vector two-point solution, the solution satisfies a one-step GPS and avoids numerical integration.

The simultaneous occurrence of BHCPs and SHCPs remains unresolved to date. The author constructs a two-point spatial solution using the boundary and termination conditions, thereby avoiding the divergence and non-convergence issues typical of traditional methods caused by nonlinearity and numerical discretization errors. This study presents a novel numerical method for solving the SHCP with unspecified initial and boundary conditions. Initially, an IHCP is decomposed into the SHCP and BHCP, both of which are extremely ill-posed problems. The LGSM method is employed to consider spatial directions, facilitating the computation of the transfer gradient in these directions and resolving the remaining boundary conditions at the boundaries. Lastly, an explicit BHCP is used in the two-point LGSM solution to determine the ICs and incorporate the ratios of the FCs to the ICs.

Section 2 presents the mathematical equation for the instantaneous temperature gradient at a specific heat transfer rod boundary, detailing its derivation and underlying principles. In Section 3, the temperature distribution function is derived by integrating

over the time direction and the temperature at the boundary is determined by further integrating over the spatial direction, thereby ensuring a complete understanding of the distribution process. Section 4 introduces the LGSM, a novel method for solving the initial temperature value, highlighting its application and advantages. Three calculation examples demonstrate the stability and reliability of the study's solution in Section 5. Finally, the study's conclusions and implications are presented in Section 6.

2. Governing Equation

The SHCP aims to estimate the external temperature of an object based on internal temperature data collected by a measuring device. The physical model is illustrated in Figure 1.

$$\frac{\partial^2 T(x,t)}{\partial x^2} = \frac{\partial T(x,t)}{\partial t},\ 0 < x < l,\ 0 < t \le t_f \tag{1}$$

with a left-side boundary condition:

$$T(0,t) = T_0(t). \tag{2}$$

and final condition:

$$T\left(x, t_f\right) = T_f(x). \tag{3}$$

where $\Omega := \left\{(x,t)\middle| 0 < x < l,\ 0 < t < t_f\right\}$, $T_0(t)$ is the temperature of the left-hand side rod, $T_f(x)$ is the final condition, l is the length of the heat conduction rod, and t_f is the terminal time.

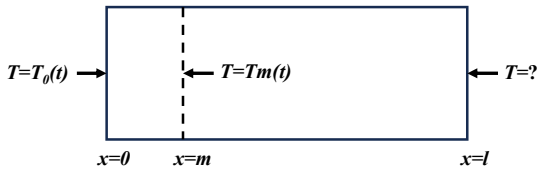


Figure 1. Schematic diagram of the SHCP.

The SHCP equation is commonly encountered in engineering applications where the goal is to infer the surface temperature of an object from internal temperature measurements. As illustrated in Figure 1, the SHCP contains an unknown $T(x = l, t)$, which cannot be solved directly. An internal temperature measurement at x_m is provided as follows:

$$T(x_m, t) = T_m(t). \tag{4}$$

Thus, the SHCP aims to determine the internal temperature field and BCs of the rod using Equations (1)–(4).

3. The Numerical Procedures

The SHCP is ill-posed because the solution does not depend continuously on the given or measured data. As displayed in Figure 2, to recover the temperature on the other side at $x = l$, Equation (1) used a semi-discretized method to discretize the quantities of $T(x,t)$ and $S(x,t)$. This yields a coupled system of ordinary differential equations and the numerical method of lines is applied for spatial integration as follows:

$$\frac{\partial T^i}{\partial x} = S^i(x),\ i = 1, \ldots, n, \tag{5}$$

$$\frac{\partial S^1(x)}{\partial x} = \frac{T^2(x) - T^1(x)}{\Delta t}, \tag{6}$$

$$\frac{\partial S^i(x)}{\partial x} = \frac{T^{i+1}(x) - T^{i-1}(x)}{2\Delta t},\ i = 2, \ldots, n-1, \tag{7}$$

$$\frac{\partial S^n(x)}{\partial x} = \frac{T^n(x) - T^{n-1}(x)}{\Delta t}. \tag{8}$$

where $\Delta t = t_f/n$ is a uniform increment and $t_i = i\Delta t$ are the discrete times. $T^i(x) = T(x, t_i)$ and $S^i(x) = S(x, t_i)$ are discretized at the nodal points in time. To enhance boundary accuracy, when a second-order central difference is employed in Equation (7) to improve overall precision, a second-order backward difference from Equation (8) is used at the final time step. To clearly describe the time domain and spatial domain integrals for SHCPs and BHCPs, the schematic diagrams of the two integrated directions are displayed in Figure 2, respectively. When solving over extended time periods and as the termination condition approaches zero, the numerical solution may diverge, which is a limitation of the method used in this study.

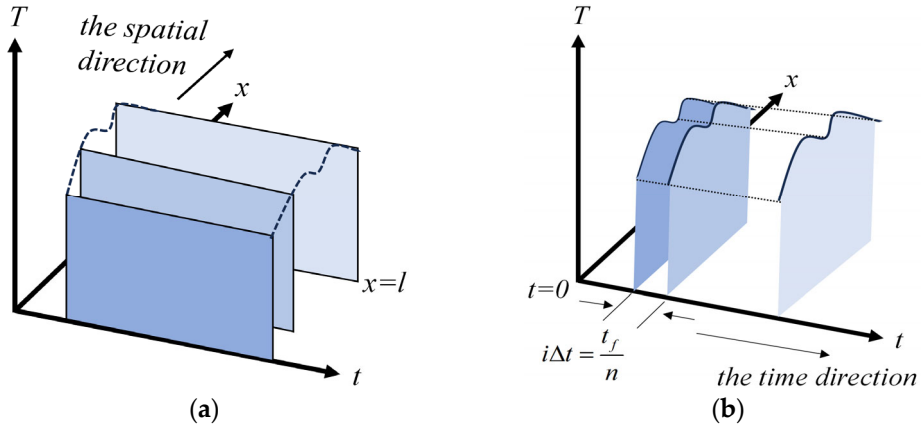


Figure 2. Schematic diagram of two integrated directions: (**a**) the spatial direction and (**b**) the time direction.

4. Mathematical Backgrounds

4.1. The GPS

To find the solution to the two-point boundary value problem, Equations (1) and (5)–(8) are reformulated as:

$$\dot{\boldsymbol{u}} = \mathbf{f}(x, \mathbf{u}), \tag{9}$$

where

$$\mathbf{u} = \begin{bmatrix} \mathbf{T} \\ \mathbf{S} \end{bmatrix}, \tag{10}$$

$$\mathbf{f} := \begin{bmatrix} \mathbf{S} \\ \mathbf{H}(x, \mathbf{T}) \end{bmatrix}. \tag{11}$$

in which $\mathbf{T} = \left(T^1, \ldots T^n\right)^t$, $\mathbf{S} = \left(S^1, \ldots S^n\right)^t$, and the superscript t denotes the transpose. $\mathbf{H}$ represents the component of Equations (6)–(8) in the right-hand side.

Liu [32] states that Equation (9) can be embedded into an augmented dynamical system:

$$\mathbf{X}' := \begin{bmatrix} \mathbf{0}_{2n\times 2n} & \frac{\mathbf{f}(x,\mathbf{u})}{\|\mathbf{u}\|} \\ \frac{\mathbf{f}^t(x,\mathbf{u})}{\|\mathbf{u}\|} & 0 \end{bmatrix} \begin{bmatrix} \mathbf{u} \\ \|\mathbf{u}\| \end{bmatrix} := \mathbf{A}\mathbf{X}. \tag{12}$$

where $\mathbf{A}$ represents an element of the Lie algebra $SO_0(2n, 1)$.

According to Liu [33], a GPS is proposed where each augmented variable $\mathbf{X}^k$ can be viewed as a point in Minkowski space M^{2n+1} ensuring that it is located on the cone:

$$\mathbf{X}^{k+1} = \mathbf{G}(k)\mathbf{X}^k. \tag{13}$$

While an exact solution of **G** is not available, an exponential mapping of **A** (k) by a closed-form expression is as follows:

$$\exp(\Delta x \mathbf{A}(\mathrm{k})) = \begin{bmatrix} \mathbf{I}_{2n} + \frac{(\overline{a}^k - 1)}{\left\|\mathbf{f}^k\right\|^2}\mathbf{f}^k\left(\mathbf{f}^k\right)^t & \frac{\overline{b}^k \mathbf{f}^k}{\left\|\mathbf{f}^k\right\|} \\ \frac{\overline{b}^k \left(\mathbf{f}^k\right)^t}{\left\|\mathbf{f}^k\right\|} & \overline{a}^k \end{bmatrix}. \tag{14}$$

where $\overline{a}^k := \cosh(\frac{\Delta x\left\|\mathbf{f}^k\right\|}{\left\|\mathbf{u}^k\right\|})$, $\overline{b}^k := \sinh(\frac{\Delta x\left\|\mathbf{f}^k\right\|}{\left\|\mathbf{u}^k\right\|})$ and $\Delta x = l/K$ is the discrete spatial size.

4.2. One-Step Lie Group Transformation

For the convenience of description, the superscripted symbols $\mathbf{u}^0$ denote the value of $\mathbf{u}$ at $x = 0$, and $\mathbf{u}^l$ the value of $\mathbf{u}$ at $x = l$. This is a one-step transformation from $\mathbf{X}^0$ to $\mathbf{X}^l$, and $\mathbf{G}(\mu)$ with a real parameter $\mu \in [0, 1]$, it can be expressed by:

$$\mathbf{G}(\mu) = \begin{bmatrix} \mathbf{I}_{2n} + \frac{(\overline{a}-1)}{\left\|\mathbf{f}_\mathrm{b}\right\|^2}\mathbf{f}_\mathrm{b}\mathbf{f}_\mathrm{b}^t & \frac{\overline{b}\mathbf{f}_\mathrm{b}}{\left\|\mathbf{f}_\mathrm{b}\right\|} \\ \frac{\overline{b}\mathbf{f}_\mathrm{b}^t}{\left\|\mathbf{f}_\mathrm{b}\right\|} & \overline{a} \end{bmatrix}. \tag{15}$$

where

$$x_b = (1-\mu)l, \tag{16}$$

$$\mathbf{u}_{\boldsymbol{b}} = \mu\mathbf{u}^0 + (1-\mu)\mathbf{u}^l, \tag{17}$$

$$\mathbf{f}_\mathrm{b} = \mathbf{f}(\mathbf{u}_\mathrm{b}, x_b), \tag{18}$$

$$\overline{a} = \cosh\left(\frac{l\left\|\mathbf{f}_\mathrm{b}\right\|}{\left\|\mathbf{u}_\mathrm{b}\right\|}\right),\ \overline{b} = \sinh\left(\frac{l\left\|\mathbf{f}_\mathrm{b}\right\|}{\left\|\mathbf{u}_\mathrm{b}\right\|}\right). \tag{19}$$

4.3. The Lie Group Shooting Equation

Let $\mathbf{G}(l) = \mathbf{G}(\mu)$, a Lie group element $\mathbf{G}(l)$ mapping $\mathbf{X}^0$ onto $\mathbf{X}^l$ is given by:

$$\begin{bmatrix} \mathbf{u}^l \\ \left\|\mathbf{u}^l\right\| \end{bmatrix} = \mathbf{G}(l)\begin{bmatrix} \mathbf{u}^0 \\ \left\|\mathbf{u}^0\right\| \end{bmatrix}. \tag{20}$$

where

$$\mathbf{G}(l) = \begin{bmatrix} \mathbf{I}_{2n} + \frac{(\overline{a}-1)}{\left\|\mathbf{F}\right\|^2}\overline{\mathbf{F}}\overline{\mathbf{F}}^\mathrm{t} & \frac{\overline{b}\overline{\mathbf{F}}}{\left\|\overline{\mathbf{F}}\right\|} \\ \frac{\overline{b}\overline{\mathbf{F}}^\mathrm{t}}{\left\|\overline{\mathbf{F}}\right\|} & \overline{a} \end{bmatrix}, \tag{21}$$

$$\overline{a} = \cosh(l\left\|\overline{\mathbf{F}}\right\|),\ \overline{b} = \sinh(l\left\|\overline{\mathbf{F}}\right\|),\ \text{and}\ \overline{\mathbf{F}} = \frac{\mathbf{f}_\mathrm{b}}{\left\|\mathbf{u}_\mathrm{b}\right\|}. \tag{22}$$

By substituting Equation (20) into Equation (21), it follows that

$$\mathbf{u}^l = \mathbf{u}^0 + \psi\overline{\mathbf{F}}, \tag{23}$$

$$\left\|\mathbf{u}^l\right\| = \overline{a}\left\|\mathbf{u}^0\right\| + \overline{b}\frac{\left[\mathbf{u}^0 \cdot \overline{\mathbf{F}}\right]}{\overline{\mathbf{F}}}. \tag{24}$$

where

$$\psi := \frac{\left[(\bar{a}-1)\overline{\mathbf{F}}\cdot\mathbf{u}^0 + \bar{b}\|\overline{\mathbf{F}}\|\|\mathbf{u}^0\|\right]}{\|\overline{\mathbf{F}}\|^2}. \tag{25}$$

By substituting Equation (23) into Equation (24), a quadratic equation for β can be derived by:

$$(1+\cos\theta)\beta^2 - \frac{2\left\|\mathbf{u}^l\right\|}{\|\mathbf{u}^0\|}\beta + 1 - \cos\theta = 0. \tag{26}$$

where

$$\beta := \exp\left(\frac{l\left\|\mathbf{u}^l - \mathbf{u}^0\right\|}{\psi}\right), \tag{27}$$

$$\cos\theta = \frac{\left(\mathbf{u}^l - \mathbf{u}^0\right)\cdot\mathbf{u}^0}{\|\mathbf{u}^l - \mathbf{u}^0\|\|\mathbf{u}^0\|}. \tag{28}$$

The solution β can be obtained from Equation (26) as follows:

$$\beta := \frac{\frac{\|\mathbf{u}^l\|}{\|\mathbf{u}^0\|} + \sqrt{\left(\frac{\|\mathbf{u}^l\|}{\|\mathbf{u}^0\|}^2\right) - (1-\cos\theta)(1+\cos\theta)}}{1+\cos\theta}. \tag{29}$$

When considering $\cos\theta = 1$ in Equation (29), a forward solution can be obtained as follows:

$$\beta_f = \frac{\left\|\mathbf{u}^l\right\|}{\|\mathbf{u}^0\|}. \tag{30}$$

However, when substituting $\cos\theta = -1$ into Equation (29), β approaches infinity and diverges. Consequently, it is possible to deduce a backward solution from Equation (26) when considering $\cos\theta = -1$ and it follows that:

$$\beta_b = \frac{(1+\cos\theta)\|\mathbf{u}^0\|}{2\|\mathbf{u}^l\|} \cong \frac{\|\mathbf{u}^0\|}{\|\mathbf{u}^l\|}. \tag{31}$$

According to Equations (30) and (31), $\beta_f = 1/\beta_b$ establish a reciprocal relationship between the $\mathbf{u}^l$ and $\mathbf{u}^0$ for forward and backward problems.

To avoid numerical divergence by Equation (32) in spatial direction integration, by inserting Equation (23) for $\overline{\mathbf{F}}$ into Equation (25), we can obtain:

$$\left\|\mathbf{u}^l - \mathbf{u}^0\right\|^2 = (\bar{a}-1)\left(\mathbf{u}^l - \mathbf{u}^0\right)\cdot\mathbf{u}^0 + \bar{b}\left\|\mathbf{u}^0\right\|\left\|\mathbf{u}^l - \mathbf{u}^0\right\|. \tag{32}$$

Dividing both sides by $\left\|\mathbf{u}^0\right\|\left\|\boldsymbol{u}^l - \boldsymbol{u}^0\right\|$, a quadratic equation for β can be derived by:

$$(1+\cos\theta)\beta^2 - 2\left(\cos\theta + \frac{\left\|\boldsymbol{u}^l - \boldsymbol{u}^0\right\|}{\|\mathbf{u}^0\|}\right)\beta - 1 + \cos\theta = 0. \tag{33}$$

From Equations (26) and (33), the solution to the quadratic equation can be obtained:

$$\beta = \frac{(\cos\theta - 1)\|\mathbf{u}^0\|}{\cos\theta\|\mathbf{u}^0\| + \left\|\mathbf{u}^l - \mathbf{u}^0\right\| - \left\|\mathbf{u}^l\right\|}. \tag{34}$$

Then from Equations (29) and (31), we can find:

$$\psi = \frac{l\left\|\mathbf{u}^l - \mathbf{u}^0\right\|}{\ln\beta}. \tag{35}$$

Therefore, the right boundary $\mathbf{u}^l$ can be obtained by using the Equations (23) and (35), and μ of $\mathbf{G}(\mu)$ is 0.5, which is decided by the left boundary $\mathbf{u}^0$ at x = 0 and $\mathbf{u}^m$.

4.4. To Estimate $\boldsymbol{u}^0$ by a Backward-in-Time Explicit Procedure

For the convenience of describing time direction integration, as displayed in Figure 2b, the subscripted symbols $\mathbf{T}_0$ denote the value of $\mathbf{T}$ at $t = 0$, and $\mathbf{T}_\mathrm{f}$ the value of $\mathbf{u}$ at $t = t_f$. According to the equation of the LGSM, we can obtain the two-point solution in the time direction as follows:

$$Z = \frac{\|\mathbf{T}_0\|}{\|\mathbf{T}_\mathrm{f}\|}. \tag{36}$$

From the previous references, we can observe the phenomenon of solution discontinuity within the computational domain. For numerical oscillation of the BHCP close to the initial condition, we use the backward second-order finite difference scheme as follows:

$$T_i = T_{i+1} + [1.5T_i - 2T_{i+1} + 0.5T_{i+2}]. \tag{37}$$

5. Numerical Examples

In this paper, the homogeneous thermally conductive material is considered the same in all cases. The noise effect is added to the measured data to test the viability and stability of this study approach. In all cases, the noise is generated by the following equation:

$$\overset{\sim}{\mathbf{T}}^{\mathrm{m}} = \mathbf{T}^{\mathrm{m}}[1 + s\delta]. \tag{38}$$

where $\mathbf{T}^{\mathrm{m}}$ represents the measured data, δ is a random number, and $-1 \le \delta \le 1$. s is the amplitude of the noise level. The noise data were generated using the rand function in MATLAB R2023a. The final noise data $\overset{\sim}{\mathbf{T}}^{\mathrm{m}}$ are applied in the numerical experiments.

5.1. Example 1

Considering the homogeneous heat transfer problem with the governing equation is as follows:

$$T_t(x,t) = T_{xx}(x,t),\ 0 < x < 1,\ 0 < t \le 1, \tag{39}$$

with an exact solution

$$T(x,t) = \exp(-t)\cos x. \tag{40}$$

According to Equation (39), the left boundary condition and measured point x_m can be obtained.

$$T(0,t) = \exp(-t). \tag{41}$$

$$T(x_m,t) = \exp(-t)\cos x_m \tag{42}$$

The Ics and right-hand BCs are obtained from the exact solutions, considering NT = 11, NS = 41, $x_m = 0.01$, and $\varepsilon = 10^{-12}$, which denote the number of grid points in the time and spatial directions, internal position measurement, and the criteria condition, respectively. The residual errors in the spatial direction at each time step are used as the convergence criterion. As seen in Figure 3, the number of LGSM iterations in this example is 4, which can satisfy the convergence requirements. The temperature at x = 1 of the numerical results

and the exact solutions are illustrated in Figure 4a. The absolute maximum errors occur at an initial time and are less than 7.99×10^{-2} as shown in Figure 4b.

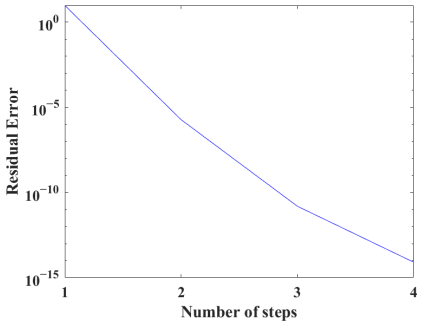
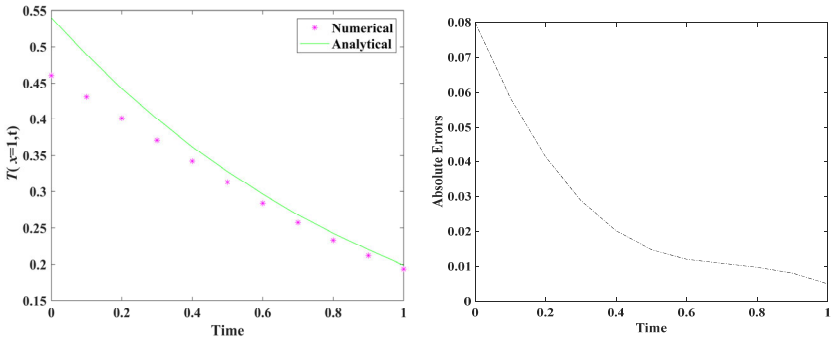


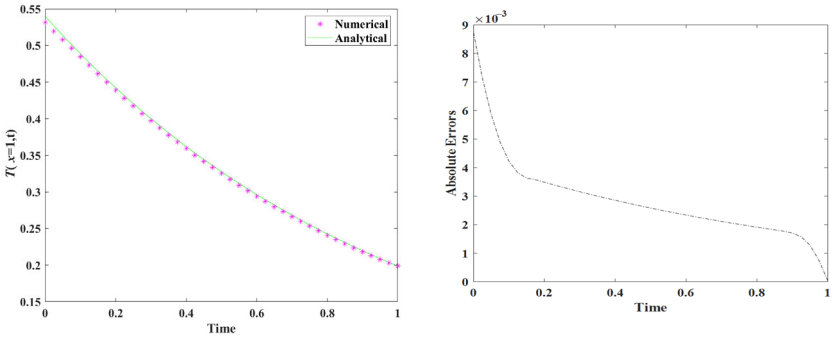
Figure 3. Example 1: The convergence plot of the LGSM.



(**a**) (**b**)

Figure 4. Example 1: Profiles of the numerical solution by (**a**) NT = 11 and NS = 41 and (**b**) the absolute errors at x = 1.

When the number of grid points in the time and space directions is increased to NT = 41 and NS = 201, the relationship between the numerical results and the exact solutions is illustrated in Figure 5a. The absolute maximum errors are demonstrated to be less than 9×10^{-3} illustrated in Figure 5b. The numerical results illustrating the effect of varying NT and NS are summarized in Table 1. The results conclude that although the integration direction is spatial, the discrete time number also depends on the numerical accuracy. When the number of spatial grids is sparse, the heat conduction gradient is almost zero, the spatial integral decomposition accuracy is low, and the errors between the numerical solution and the analytical value are enormous.



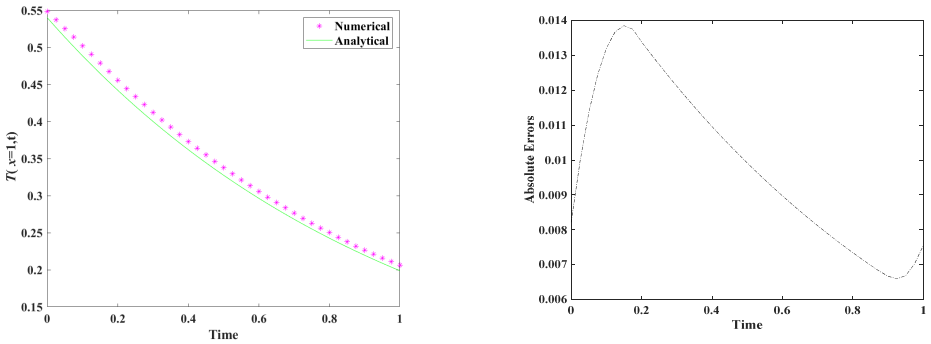
(**a**) (**b**)

Figure 5. Example 1: Profiles of numerical solution by (**a**) NT = 41 and NS = 201 and (**b**) the absolute errors at x = 1.

Table 1. Example 1: Maximum absolute errors under different time and space discretizations.

NT	NS	Maximum Absolute Errors
11	41	7.99×10^{-2}
	101	6.86×10^{-2}
	201	6.49×10^{-2}
41	41	2.52×10^{-2}
	101	1.28×10^{-2}
	201	8.72×10^{-3}

To assess numerical stability, we consider a noise effect of s = 1%. Using NT = 41 and NS = 201, the number of iterations for the LGSM is 4. The numerical results and absolute errors are displayed in Figure 6. The maximum absolute errors are less than 1.10×10^{-2}. The accuracy of the numerical solutions can be enhanced by increasing the number of time discretization in the same number of grids. When 1% noise is added to the measurement point, the errors between the numerical and exact solutions can still be maintained at order 10^{-2}.



(**a**) (**b**)

Figure 6. Example 1: Profiles of the numerical solution by (**a**) NT = 41 and NS = 201 and (**b**) the absolute errors at $x = 1$ under noise level $s = 1\%$.

5.2. Example 2

Considering a heat transfer problem, the equation is as follows:

$$T_t(x,t) = T_{xx}(x,t),\ 0 < x < 1,\ 0 < t \leq 1, \tag{43}$$

with an exact solution

$$T(x,t) = exp(-t)sinx + x^2 + 2t. \tag{44}$$

Homogeneous boundary conditions:

$$T(0,t) = 2t, T(1,t) = \exp(-t)sin1 + 1^2 + 2t. \tag{45}$$

Final condition:

$$T\left(x,t_f\right) = \exp\left(-t_f\right)sinx + x^2 + 2t_f. \tag{46}$$

Setting the following parameters: $l = 1$, $t_f = 1$, $x_m = 0.1$, and $\varepsilon = 10^{-12}$, considering that NT = 11 and NS = 41, the iterative number of LGSM is 5, and satisfactory accuracy can be obtained, as displayed in Figure 7. The numerical results and absolute errors are displayed in Figure 8. The maximum absolute errors are less than 1.23×10^{-1}.

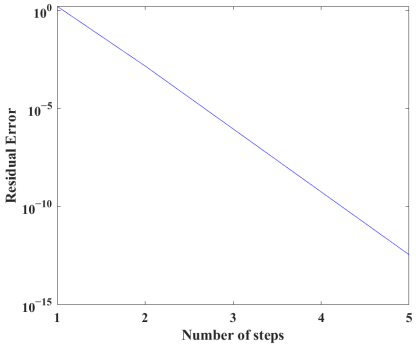
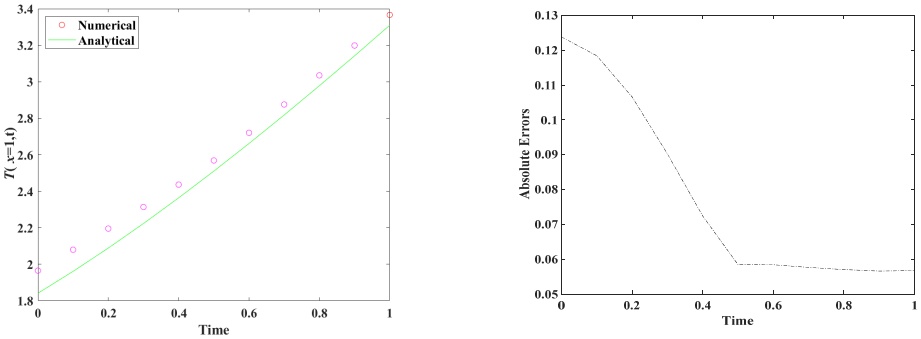


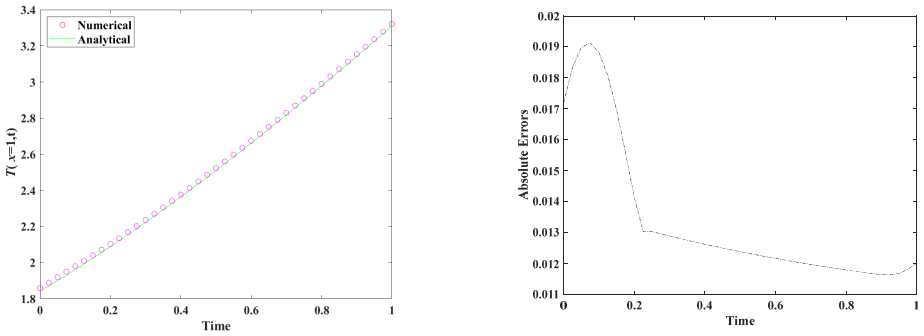
Figure 7. Example 2: The convergence plot of the LGSM.



(**a**) (**b**)

Figure 8. Example 2: Profiles of the numerical solution by (**a**) NT = 11 and NS = 41 and (**b**) the absolute errors at x = 1.

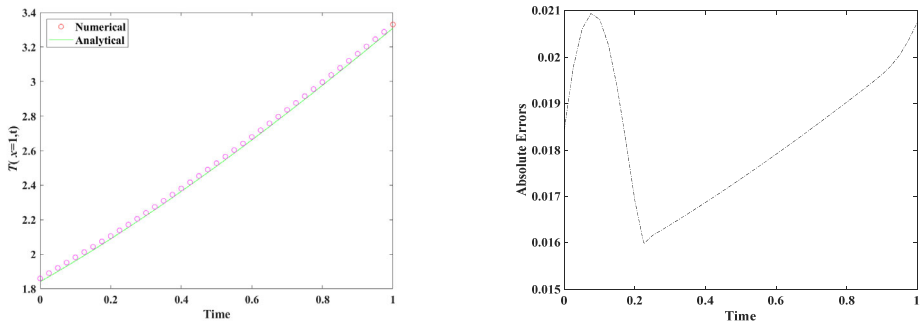
When NT = 41 and NS = 201, the numerical results and absolute errors are as displayed in Figure 9. The maximum absolute errors are less than 1.91×10^{-2}.



(**a**) (**b**)

Figure 9. Example 2: Profiles of the numerical solution by (**a**) NT = 41 and NS = 201 and (**b**) the absolute errors at x = 1.

When further considering a noise effect s = 1%, using NT = 41 and NS = 201, the numerical results and absolute errors are as displayed in Figure 10. The maximum absolute errors are less than 2.09×10^{-2}.



(**a**) (**b**)

Figure 10. Example 2: Profiles of numerical solutions by (**a**) NT = 41 and NS = 201 and (**b**) the absolute errors at x = 1 under noise level s = 1%.

Therefore, Table 2 summarizes the maximum absolute errors under various time and spatial discretizations. With identical time discretization conditions, increasing the spatial discretization degree leads to a smaller numerical absolute error. As both time and spatial discretization increase, the numerical solution tends to converge toward the exact solution. The time step size is a critical factor that significantly affects the numerical absolute errors.

Table 2. Example 2: Maximum absolute errors under different time and space discretizations.

NT	NS	Maximum Absolute Errors
11	41	1.23×10^{-1}
	101	7.55×10^{-2}
	201	5.97×10^{-2}
	501	5.02×10^{-2}
41	41	7.83×10^{-2}
	101	3.25×10^{-2}
	201	1.91×10^{-2}
	501	1.11×10^{-2}

5.3. Example 3

Consider a heat conduction problem with a closed-form solution for

$$T(x,t) = \frac{1}{\sqrt{1+4t}} \exp\left(-\frac{x^2}{1+4t}\right). \tag{47}$$

The initial conditions are obtained $T(x) = \exp(-x^2)$ when $t = 0$, and the temperature history measured at location x_m is exactly

$$T(x_m,t) = \frac{1}{\sqrt{1+4t}} \exp\left(-\frac{x_m^2}{1+4t}\right). \tag{48}$$

Setting the following parameters: $l = 1$, $t_f = 1$, $x_m = 0.01$ and $\varepsilon = 10^{-12}$. Considering that NT = 11, NS = 41 according to the LGSM, the number of iterations of LGSM is 4, and satisfactory accuracy can be obtained, as displayed in Figure 11. The numerical results and absolute errors are displayed in Figure 12. The maximum absolute errors are less than 8.33×10^{-2}.

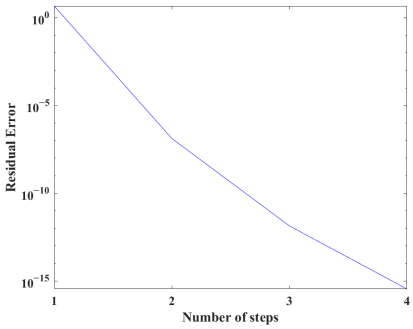
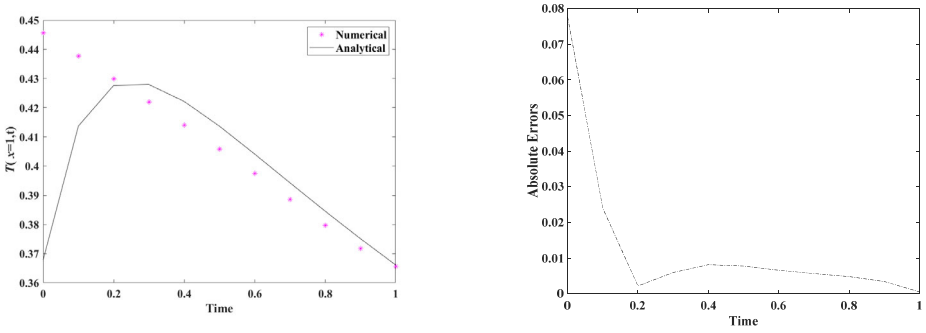


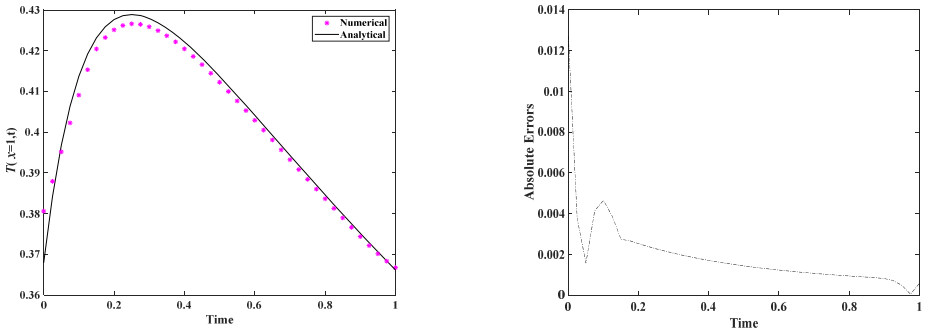
Figure 11. Example 3: The convergence plot of the LGSM.



(**a**) (**b**)

Figure 12. Example 3: Profiles of the numerical solution by (**a**) NT = 11 and NS = 41 and (**b**) the absolute errors at x = 1.

When NT = 41 and NS = 201, the numerical results and absolute errors are displayed in Figure 13. The maximum absolute errors are less than 1.27×10^{-2}. When considering a noise effect, s = 1%. Using NT = 41 and NS = 201, the numerical results and absolute errors are less than 2.71×10^{-2}. The maximum absolute errors are displayed in Figure 14.

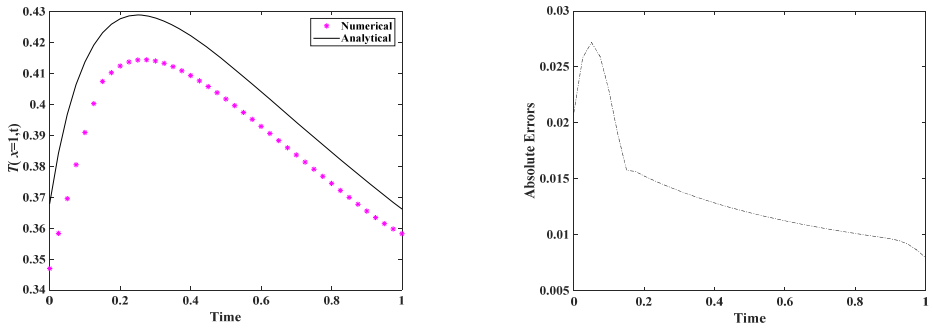


(**a**) (**b**)

Figure 13. Example 3: Profiles of the numerical solution by (**a**) NT = 41 and NS = 201 and (**b**) the absolute errors at x = 1.

Therefore, the maximum absolute errors under various time and spatial discretizations are summarized in Table 3. Through the combination of time and space discretization, a set of numerical solutions with better accuracy can be obtained and better accuracy can be obtained.

As demonstrated in the previous two examples, when accounting for measurement noise, maintaining the spatial discrete number fixed and increasing the discrete time number can help keep the absolute errors within a certain level 1×10^{-2}. Whether the exact solution is expressed in exponential or polynomial form, the method utilized in this study can attain stable numerical accuracy.



(**a**) (**b**)

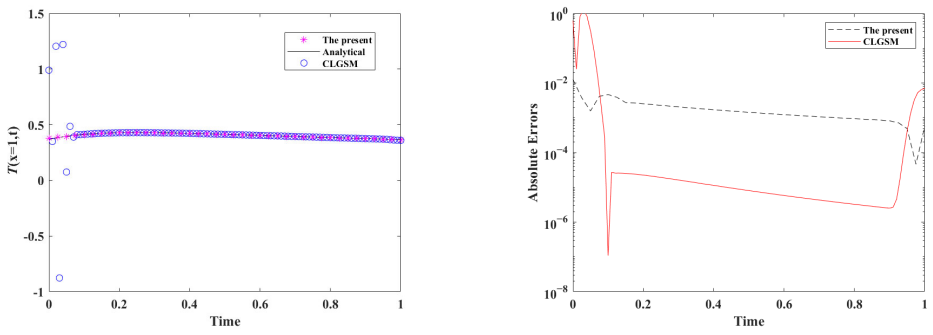
Figure 14. Example 3: Profiles of numerical solutions by (**a**) NT = 41 and NS = 201 and (**b**) the absolute errors at x = 1 under noise level s = 1%.

Table 3. Example 3: Maximum absolute errors under different time and space discretizations.

NT	NS	Maximum Absolute Errors
11	41	7.76×10^{-1}
	101	8.51×10^{-2}
	201	8.76×10^{-2}
	501	8.91×10^{-2}
41	41	1.80×10^{-2}
	101	8.32×10^{-2}
	201	1.27×10^{-2}
	501	1.53×10^{-2}

In order to emphasize the stability of the proposed method, the right-hand side boundary condition is solved using the two-stage conventional Lie group shooting method (CLGSM) and the one-stage approach of the present method. Considering the same parameters, the results are as follows:

Figure 15 presents a comparison of the numerical solutions and maximum absolute errors between the present LGSM and the CLGSM. The results indicate that the CLGSM produces diverging and unstable oscillations in the computed values as time approaches zero, whereas the present LGSM method effectively addresses this issue, as illustrated in Figure 15a. The maximum absolute error of the present LGSM method is approximately 10^{-2}, while that of the CLGSM is around 1, as shown in Figure 15b. The primary reason for this discrepancy is that the present LGSM employs a single-stage backward integration method, which ensures the stability of the integration process. In contrast, the CLGSM exhibits oscillatory divergence as time approaches zero, leading to larger errors. Consequently, the present LGSM demonstrates superior solution stability.



(**a**) (**b**)

Figure 15. Profiles of (**a**) the numerical solution obtained by the present LGSM, the analytical solution, and the CLGSM, and (**b**) the absolute errors at x = 1 computed by the present LGSM and the CLGSM.

6. Conclusions

This study presents a robust framework for addressing heat conduction problems involving incomplete or noisy data, with specific applications in marine engineering. By reformulating the problem and employing advanced numerical techniques, we provide an effective solution for determining missing boundary conditions within computational heat conduction domains. The IHCP is systematically divided into two sub-problems: the SHCP and the BHCP. Initially, the heat conduction gradient is calculated by integrating the LGSM along the spatial direction. At each time step, the temperature distribution in the computational domain and the right-boundary condition are obtained. Subsequently, the SHCP is treated as the BHCP and backward time integration is performed.

The results demonstrate that simply altering the integration direction in conventional methods does not resolve numerical divergence issues. The presence of only a left boundary and a measurement boundary can lead to a multi-solution phenomenon due to the two-point nature of the problem. Numerical oscillations arise as the methods encounter multiple solutions while satisfying energy conservation constraints. By leveraging the two-point solution and closing the Lie group, the computational domain's temperature at each time step is accurately determined through backward time integration. This numerical approach is highly efficient and reliable, requiring no regularization techniques to mitigate numerical instability. As a result, the proposed algorithm for solving inverse heat conduction problems outperforms existing methods in terms of effectiveness, stability, and accuracy. Based on these facts, the current research can simplify two- or three-dimensional problems into one-dimensional, two-point solutions along the time dimension. By employing single-point reverse integration in the time dimension, the temperature at each time step can be used to construct a two-point solution to derive the initial temperature. In future work, the LGSM can be extended to variable-coefficient heat conduction problems using the vector-boundary two-point solution.

Author Contributions: C.-C.T. contributed to the conception and supervision of the work (conceptualization, resources, methodology, writing—original draft), collected and analyzed the data, and interpreted the results. C.-F.S. contributed to the conception of the work (project administration, software). J.-H.S. contributed to the writing and supervision of the work (writing—review and editing, software, project administration). Y.-W.C. contributed to the writing, design and validation of the work (writing—editing, validating, and visualizing the data), and the funding acquisition. All authors have read and agreed to the published version of the manuscript.

Funding: The corresponding author would like to thank the National Science and Technology Council of Taiwan for their financial support (grant number NSTC 112-2221-E-019-032).

Data Availability Statement: No new data were generated for this study. All data supporting the reported results are contained within the article.

Conflicts of Interest: The authors declare that there are no conflicts of interest regarding the publication of this paper.

References

1. Duda, P.; Taler, J. A new method for identification of thermal boundary conditions in water-wall tubes of boiler furnaces. *Int. J. Heat Mass Transf.* **2009**, *52*, 1517–1524. [CrossRef]
2. Maniruzzaman, M.; Sisson, R.D., Jr. Heat transfer coefficients for quenching process simulation. *J. Phys. IV* **2004**, *120*, 521–528. [CrossRef]
3. O'donnell, R.N.; Powell, T.R.; Filipi, Z.S.; Hoffman, M.A. Estimation of thermal barrier coating surface temperature and heat flux profiles in a low temperature combustion engine using a modified sequential function specification approach. *J. Heat Transf.-Trans. ASME* **2017**, *139*, 041201. [CrossRef]
4. Hadamard, J. *Lectures on Cauchy's Problem in Linear Partial Differential Equations*; Dover Publications: New York, NY, USA, 1953.
5. Kronberg, A.E.; Benneker, A.H.; Westerterp, K.R. Notes on wave theory in heat conduction: A new boundary condition. *Int. J. Heat Mass Transf.* **1998**, *41*, 127–137. [CrossRef]

6. Stefanyuk, E.V.; Kudinov, V.A. Approximate analytic solution of heat conduction problems with a mismatch between initial and boundary conditions. *Russ. Math.* **2010**, *54*, 55–61. [CrossRef]
7. Cao, K.; Lesnic, D.; Liu, J. Simultaneous reconstruction of space-dependent heat transfer coefficients and initial temperature. *J. Comput. Appl. Math.* **2020**, *375*, 112800. [CrossRef]
8. Beck, J.V.; Blackwell, B.; St. Clair, C.R. *Inverse Heat Conduction: Ill-Posed Problem*; Wiley: New York, NY, USA, 1985.
9. Carasso, A.S. Slowly divergent space marching schemes in the inverse heat conduction problem. *Numer. Heat Tranf. B-Fundam.* **1993**, *23*, 111–126. [CrossRef]
10. Murio, D.A. The mollification method and the numerical solution of the inverse heat conduction problem by finite differences. *Comput. Math. Appl.* **1989**, *17*, 1385–1396. [CrossRef]
11. Murio, D.A. *The Mollification Method and the Numerical Solution of Ill-Posed Problems*; John Wiley & Sons: New York, NY, USA, 1993.
12. Al-Khalidy, N. A general space marching algorithm for the solution of two-dimensional boundary inverse heat conduction problems. *Numer. Heat Tranf. B-Fundam.* **1998**, *34*, 339–360. [CrossRef]
13. Eldén, L. *Numerical Solution of the Sideways Heat Equation*; SIAM: Philadelphia, PA, USA, 1995.
14. Krutz, G.W.; Schoenhals, R.J.; Horc, P.S. Application of finite element method to the inverse heat conduction problem. *Numer. Heat Tranf. B-Fundam.* **1978**, *1*, 489–498. [CrossRef]
15. Mobtil, M.; Bougeard, D.; Russeil, S. Experimental study of inverse identification of unsteady heat transfer coefficient in a fin and tube heat exchanger assembly. *Int. J. Heat Mass Transf.* **2018**, *125*, 17–31. [CrossRef]
16. Reinhardt, H.J. A numerical method for the solution of two-dimensional inverse heat conduction problems. *Int. J. Numer. Methods Eng.* **1991**, *32*, 363–383. [CrossRef]
17. Brebbia, C.A. Applications of the boundary element method for heat transfer problems. *Rev. Gén. Therm.* **1985**, *24*, 353–361.
18. Pasquetti, R.; Le Niliot, C. Boundary element approach for inverse heat conduction problems: Application to a bidimensional transient numerical experiment. *Numer. Heat Tranf. B-Fundam.* **1991**, *20*, 169–189. [CrossRef]
19. Ingham, D.B.; Yuan, Y.; Han, H. The boundary-element method for an improperly posed problem. *IMA J. Appl. Math.* **1991**, *47*, 61–79. [CrossRef]
20. Kurpisz, K.; Nowak, A.J. BEM approach to inverse heat conduction problems. *Eng. Anal. Bound. Elem.* **1992**, *10*, 291–297. [CrossRef]
21. Lesnic, D.; Elliott, L.; Ingham, D.B. The solution of an in-verse heat conduction problem subject to the specification of energies. *Int. J. Heat Mass Transf.* **1998**, *41*, 25–32. [CrossRef]
22. Al-Najem, N.M.; Osman, A.M.; El-Refaee, M.M.; Khanafer, K.M. Two dimensional steady-state inverse heat conduction problems. *Int. Commun. Heat Mass Transf.* **1998**, *25*, 541–550. [CrossRef]
23. Singh, K.M.; Tanaka, M. Dual reciprocity boundary element analysis of inverse heat conduction problems. *Comput. Meth. Appl. Mech. Eng.* **2001**, *190*, 5283–5295. [CrossRef]
24. Hon, Y.C.; Wei, T. A meshless computational method for solving inverse heat conduction problems. *WIT Trans. Model. Simul.* **2002**, *32*, 135–144.
25. Hon, Y.C.; Wei, T. The method of fundamental solution for solving multidimensional inverse heat conduction problems. *CMES-Comp. Model. Eng. Sci.* **2005**, *7*, 119–132. [CrossRef]
26. Reginska, T. Application of wavelet shrinkage to solving the sideways heat equation. *BIT Numer. Math.* **2001**, *41*, 1101–1110. [CrossRef]
27. Qiu, C.Y.; Fu, C.L.; Zhu, Y.B. Wavelets and regularization of the sideways heat equation. *Comput. Math. Appl.* **2003**, *46*, 821–829. [CrossRef]
28. Berntsson, F. Sequential solution of the sideways heat equation by windowing of the data. *Inverse Probl. Eng.* **2003**, *11*, 91–103. [CrossRef]
29. Cheng, W.; Liu, Y.L.; Yang, F. A modified regularization method for a spherically symmetric inverse heat con-duction problem. *Symmetry* **2022**, *14*, 2102. [CrossRef]
30. Lin, S.M.; Chen, C.K.; Yang, Y.T. A modified sequential approach for solving inverse heat conduction problems. *Int. J. Heat Mass Transf.* **2004**, *47*, 2669–2680. [CrossRef]
31. Zhang, H.; Zou, J.; Xiao, P. Sequential regularization method for the identification of mold heat flux during continuous casting using inverse problem solutions techniques. *Metals* **2023**, *13*, 1685. [CrossRef]
32. Liu, C.S. Cone of non-linear dynamical system and group preserving schemes. *Int. J. Non-Linear Mech.* **2001**, *36*, 1047–1068. [CrossRef]
33. Liu, C.S. Group preserving scheme for backward heat conduction problems. *Int. J. Heat Mass Transf.* **2004**, *47*, 2567–2576. [CrossRef]
34. Liu, C.S.; Chang, C.W.; Chang, J.R. Past cone dynamics and backward group preserving schemes for backward heat conduction problems. *CMES-Comp. Model. Eng. Sci.* **2006**, *12*, 67–82. [CrossRef]

35. Chang, C.W.; Liu, C.S.; Chang, J.R. A new shooting method for quasi-boundary regularization of multi-dimensional backward heat conduction problems. *J. Chin. Inst. Eng.* **2009**, *32*, 307–318. [CrossRef]
36. Chang, J.R.; Liu, C.S.; Chang, C.W. A new shooting method for quasi-boundary regularization of backward heat conduction problems. *Int. J. Heat Mass Transf.* **2007**, *50*, 2325–2332. [CrossRef]
37. Liu, C.S. The Lie-group shooting method for nonlinear two-point boundary value problems exhibiting multiple solutions. *CMES-Comp. Model. Eng. Sci.* **2006**, *13*, 149–164. [CrossRef]
38. Chen, Y.W. A modified Lie-group shooting method for multi-dimensional backward heat conduction problems under long time span. *Int. J. Heat Mass Transf.* **2018**, *127*, 948–960. [CrossRef]
39. Chen, Y.W. A backward-forward Lie-group shooting method for nonhomogeneous multi-dimensional back-ward heat conduction problems under a long time span. *Int. J. Heat Mass Transf.* **2019**, *133*, 226–246. [CrossRef]
40. Chen, Y.W. Simultaneous determination of the heat source and the initial data by using an explicit Lie-group shooting method. *Numer. Heat Tranf. B-Fundam.* **2019**, *75*, 239–264. [CrossRef]
41. Chang, Y.S.; Chen, Y.W.; Liu, C.S.; Chang, J.R. A non-iteration solution for solving the backward-in-time two-dimensional Burgers' equation with a large Reynolds number. *J. Mar. Sci. Technol.-Taiwan* **2022**, *30*, 75–85.
42. Liu, C.S. An Iterative Method to Recover the Heat Conductivity Function of a Nonlinear Heat Conduction Equation. *Numer. Heat Tranf. B-Fundam.* **2013**, *65*, 80–101. [CrossRef]
43. Liu, C.S. Using a Lie-group adaptive method for the identification of a nonhomogeneous conductivity function and unknown boundary data. *CMC-Comput. Mat. Contin.* **2011**, *21*, 17–39. [CrossRef]
44. Liu, C.S. A Lie-group adaptive method to identify spatial-dependence heat conductivity coefficients. *Numer. Heat Tranf. B-Fundam.* **2011**, *60*, 305–323. [CrossRef]
45. Liu, C.S. An LGEM to identify time-dependent heat conductivity function by an extra measurement of temperature gradient. *CMC-Comput. Mat. Contin.* **2008**, *7*, 81–95. [CrossRef]

Disclaimer/Publisher's Note: The statements, opinions and data contained in all publications are solely those of the individual author(s) and contributor(s) and not of MDPI and/or the editor(s). MDPI and/or the editor(s) disclaim responsibility for any injury to people or property resulting from any ideas, methods, instructions or products referred to in the content.